J. Fluid Mech. (2024), *vol*. 980, A36, doi:10.1017/jfm.2024.26

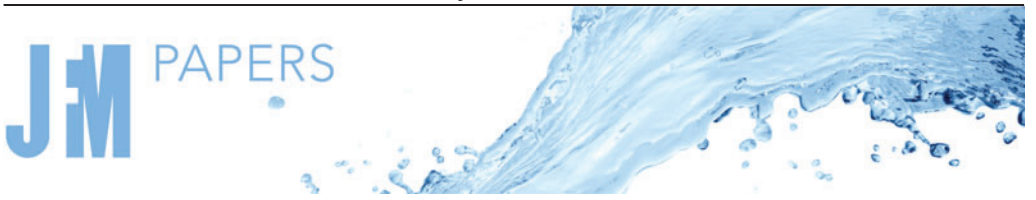

Dynamics of collapse of free-surface bubbles: effects of gravity and viscosity

Sangeeth Krishnan[1],†, **Baburaj A. Puthenveettil**[2] **and E.J. Hopfinger**[3]

[1]International Centre for Theoretical Sciences, Tata Institute of Fundamental Research, Bengaluru 560 089, India

[2]Department of Applied Mechanics, Indian Institute of Technology Madras, Chennai 600 036, India

[3]LEGI-CNRS, Université Grenoble Alpes, CS40700, 38052 Grenoble, France

(Received 28 March 2023; revised 18 November 2023; accepted 30 December 2023)

The rupture of the thin film at the top of a bubble at a liquid–gas interface leads to an axisymmetric collapse of the bubble cavity. We present scaling laws for such a cavity collapse, established from experiments conducted with bubbles spanning a wide range of Bond ($10^{-3} < Bo \leq 1$) and Ohnesorge numbers ($10^{-3} < Oh < 10^{-1}$), defined with the bubble radius R. The cavity collapse is a capillary-driven process, with a dependency on viscosity and gravity, affecting respectively, precursory capillary waves on the cavity boundary and the static bubble shape. The collapse is characterised by the normal interface velocity (U_n) and by the tangential wave propagation velocity of the kink (U_t), defined by the intersection of the concave cavity boundary formed after the rupture of the thin film with the convex boundary of the bubble cavity. During the collapse, U_t remains constant and is shown to be $U_t = 4.5U_c\mathcal{W}_R$, where U_c is the capillary velocity and $\mathcal{W}_R(Oh, Bo) = (1 - \sqrt{Oh\mathscr{L}})^{-1/2}$ is the wave resistance factor due to the precursory capillary waves, with $\mathscr{L}(Bo)$ being the path correction of the kink motion. The movement of the kink in the normal direction is part of the inward shrinkage of the whole cavity due to the sudden reduction of gas pressure inside the bubble cavity after the thin film rupture. This normal velocity is shown to scale as U_c in the equatorial plane, while at the bottom of the cavity $\bar{U}_{nb} = U_c(Z_c/R)(\mathcal{W}_R/\mathscr{L})$, where $Z_c(Bo)$ is the static cavity depth. The filling rate of the cavity, which remains a constant throughout the collapse, is shown to be entirely determined by the shrinking velocity and scales as $Q_T \simeq 2\pi RZ_cU_c$. From Q_T we recover the jet velocity scaling, thereby relating the cavity collapse with the jet velocity scaling.

Key words: capillary waves, capillary flows

† Present address: National Institute of Technology Calicut. Email address for correspondence: sangeethkrishnan@nitc.ac.in

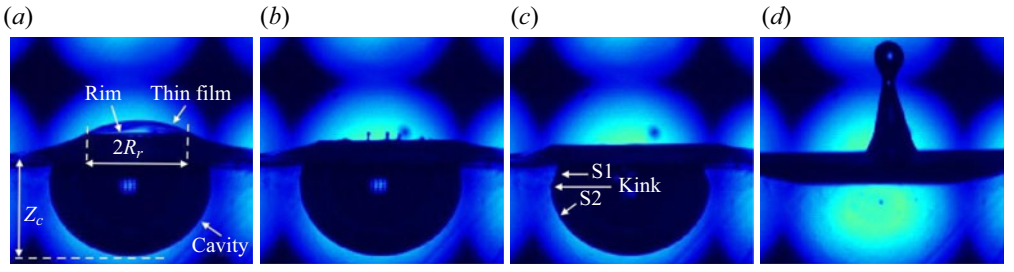

Figure 1. Stages of bubble collapse at a liquid surface. (*a*) Static bubble in water with a radius $R \approx 2$ mm; (*b*) rupturing of thin film; (*c*) beginning of the cavity collapse; (*d*) jet at the free surface. The time gaps between the images are of the order of 10^{-4} s.

1. Introduction

A bubble at a liquid–gas interface is characterised by a cavity, capped from above by a spherical thin film, and joined at a circular rim, as shown in figure 1(*a*). The rupture of the thin film leaves an unstable cavity at the interface, which collapses axisymmetrically and generates a high-velocity jet (Woodcock *et al.* 1953; Kientzler *et al.* 1954); figure 1 shows an image sequence of a bubble bursting at the free surface. The bursting of these free-surface bubbles is an important transport mechanism in mass transport from the liquid surfaces to the ambient air in air–sea exchange and in the spread of pathogens (Blanchard 1963; MacIntyre 1972; Spiel 1995; Walls, Henaux & Bird 2015; Joung, Ge & Buie 2017; Sampath *et al.* 2019; Yang *et al.* 2023). Bubble bursting has also been investigated in connection with the reverse mass transport observed in the mixing of oil spills in the ocean (Feng *et al.* 2014), and in the context of the creation of intense stress zones in bioreactors (Boulton-Stone & Blake 1993; Walls *et al.* 2017).

Most of these studies on free-surface bubble collapse have focused on the dynamics of the ensuing jetting. The general consensus on jetting is that, when Ohnesorge number $Oh = \mu/\sqrt{\sigma\rho R} < 0.037$, the jet velocity U_j scales with the capillary velocity $U_c = \sqrt{\sigma/\rho R}$ (see table 1 for the definitions of symbols), provided, the bubbles are small, such that Bond number $Bo = \rho g R^2/\sigma < 0.1$. However, for larger bubbles, when $Bo > 0.1$, the jet velocity can deviate substantially from the capillary velocity U_c due to gravity effects (Gañán Calvo 2017, 2018; Krishnan, Hopfinger & Puthenveettil 2017; Deike *et al.* 2018; Gordillo & Rodríguez-Rodríguez 2019). A jet Weber number scaling, $We_j = \rho {U_j}^2 R/\sigma \sim (Z_c/R)^2$, proposed by Krishnan *et al.* (2017), explains the effect of gravity on jet velocity through the static depth of the bubble cavity Z_c (see figure 1*a*), where Z_c is a function of Bond number, as given by Puthenveettil *et al.* (2018). Significant progress has been made recently towards the theoretical understanding of the jet dynamics (Lai, Eggers & Deike 2018; Blanco-Rodríguez & Gordillo 2020; Gañán Calvo & López-Herrera 2021), and accurate predictions have been made for the sizes of ejected first drops from the jets for a wide range of bubble radii (Gañán Calvo & López-Herrera 2021; Gañán-Calvo 2023).

The cavity collapse dynamics associated with this jetting is complex, with the velocities being at least an order of magnitude less than the jet velocity (Krishnan & Puthenveettil 2015; Gañán Calvo & López-Herrera 2021). As seen in the images of surface bubble cavity collapse (figure 1), after the thin surface film rupture, the hole expansion creates a concave boundary (as seen from the liquid side), S1 in figure 1(*c*) (Krishnan, Puthenveettil & Hopfinger 2020), with the formation of a kink at its intersection with the convex cavity shape, S2 in figure 1(*c*). The kink propagates tangentially along the boundary with velocity U_t, while at the same time, the cavity shrinks with a velocity U_n normal to the boundary

	μ mPa s	ρ kg m^{-3}	σ N m^{-1}	R mm	Bo	Oh	t_c ms	U_c m s^{-1}
Water	1.005	1000	0.072	0.175–4.1	0.004–2.27	0.0019–0.009	0.3–30.7	0.64–0.13
Ethanol	1.144	789	0.022	0.19–1.16	0.013–0.47	0.008–0.02	0.5–7.5	0.38–0.16
2-propanol	2.073	781	0.018	1.46–2.41	0.9–2.4	0.011–0.014	11.6–24.6	0.13–0.1
GW48 (30 °C)	3.9	1115	0.068	0.42–3.4	0.029–1.9	0.0076–0.021	1.1–25.4	0.38–0.13
GW48 (20 °C)	5.5	1120	0.068	0.81–1.96	0.1–0.62	0.014–0.022	3–11.1	0.27–0.18
GW55 (20 °C)	8	1140	0.067	0.71–2.3	0.08–0.88	0.019–0.035	2.5–14.4	0.29–0.16
GW68 (20 °C)	12.414	1170	0.066	0.48–2.3	0.04–0.89	0.03–0.064	1.4–14.7	0.34–0.16
GW72 (20 °C)	16.616	1181	0.064	0.6–3.6	0.063–2.4	0.032–0.079	2–29.3	0.3–0.12
GW89 (20 °C)	185.3	1232	0.064	1.7	0.54	0.52	9.6	0.18

Table 1. The properties of the fluids used in the experiments and the corresponding dimensionless parameters. The fluid properties of surface tension, density and dynamic viscosity are denoted by σ, ρ and μ, respectively, while g is the acceleration due to gravity. The Bond number $Bo = \rho g R^2/\sigma$, the Ohnesorge number $Oh = \mu/\sqrt{\sigma\rho R}$, the capillary time scale $t_c = \sqrt{\rho R^3/\sigma}$ and the capillary velocity scale $U_c = \sqrt{\sigma/\rho R}$.

due to the excess capillary pressure after the gas pressure drops when the cavity opens. Capillary waves, similar to the waves observed earlier in steep gravity waves (Perlin, Lin & Ting 1993) and Faraday waves (Das & Hopfinger 2008; Puthenveettil & Hopfinger 2009), move ahead of the main (kink) capillary wave (see figure 3). Viscous damping of these precursory capillary waves is proportional to $Oh^{1/2}$, which is valid till the complete suppression of the waves (Krishnan *et al.* 2017; Gordillo & Rodríguez-Rodríguez 2019). Such progressive viscous damping of these waves results in an increase in the jet velocity up to $Oh \approx 0.02$, beyond which the jet velocity decreases (Ghabache *et al.* 2014). This complex dependence of jet velocity on Oh for a broad range of Oh and Bo, including the critical $Oh \approx 0.03$, after which viscosity acts on the cavity size, was first explained by Gañán Calvo & López-Herrera (2021) as a nonlinear smooth transition.

While the stages of collapse described above, and shown in figure 1, have been well identified (MacIntyre 1972; Duchemin *et al.* 2002; Lee *et al.* 2011; Brasz *et al.* 2018), quantitative information and scaling laws for the velocities of collapse, and the related mass fluxes are not available. The two-dimensionality of the moving kink, and the lack of top-down symmetry of the interface during flow convergence prevent the use of one-dimensional, Rayleigh–Plesset equation based models, often used to study the cavities at the free surface formed by impacting objects (Oguz & Prosperetti 1993; Burton, Waldrep & Taborek 2005; Bartolo, Josserand & Bonn 2006; Bergmann *et al.* 2006; Duclaux *et al.* 2007). Even though it has been found that the kink moves with a constant velocity, proportional to the capillary velocity (Krishnan & Puthenveettil 2015; Krishnan *et al.* 2017; Gordillo & Rodríguez-Rodríguez 2019), its dependency on Oh, through precursor capillary waves, and on Bo through the total path length, has not been addressed in any detail. The effect of precursory capillary waves on jet velocity has been extensively studied (Ghabache *et al.* 2014; Gañán Calvo 2017; Krishnan *et al.* 2017; Deike *et al.* 2018; Gañán Calvo 2018; Gañán Calvo & López-Herrera 2021; Gordillo & Rodríguez-Rodríguez 2019; Blanco-Rodríguez & Gordillo 2021). However, the effect of these waves on the collapsing cavity surface has not been addressed.

Most other studies (Gañán Calvo 2017, 2018; Ismail *et al.* 2018; Lai *et al.* 2018; Blanco-Rodríguez & Gordillo 2021) consider only the dynamics of flow convergence in a small region at the cavity bottom, where viscosity also dictates the length scale. Gordillo & Rodríguez-Rodríguez (2019), Blanco-Rodríguez & Gordillo (2021) and Gordillo &

Blanco-Rodríguez (2023) assumed a purely horizontal and radially inward inertial flow during the flow convergence at the cavity bottom and modelled the flow using a vertical array of sinks placed along the meridian centre line, with the length of the array being determined by the size of the bubble and the wavelength of the capillary waves moving ahead of the kink. Lai *et al.* (2018) showed that the shapes of the collapsing cavity are self-similar, with a capillary–inertial $|t_s - t|^{2/3}$ scaling, where $t_s - t$ is the time to the singularity and t_s being the instant of fluid convergence at the cavity bottom. This is similar to the scaling of Zeff *et al.* (2000) in Faraday wave collapse. However, such a self-similarity only holds for $0.014 < Oh \leq 0.04$ and small Bond numbers ($Bo \ll 0.1$), when precursory capillary waves are absent.

An important exception to these local convergence studies is the analysis of streamlines for the entire fluid domain by Gañán Calvo & López-Herrera (2021), wherein the authors show why a global analysis of cavity collapse is necessary for the complete understanding of the focusing zone and jet formation. Gañán Calvo & López-Herrera (2021) proposed the spherically averaged velocity during the flow convergence to scale as $W \sim (V_\mu/Oh_L)\psi(Oh, Oh_L, Bo)$, where $V_\mu = \sigma/\mu$, and Oh_L is the Ohnesorge number based on the length scale at the bottom of the cavity at flow convergence; in the limit $Oh \ll 0.04$, W tends to the capillary velocity U_c (Gañán Calvo 2017, 2018). These fluid flow velocity based scalings may not match with the scalings based on the interface velocities, which we study here in the present work, to determine explicit relations for the normal velocity at the bottom of the cavity as a function of Oh and Bo. As we mentioned above, and discuss in detail later, we show that the cavity surface during flow convergence at the bottom has both radial (spherical) and tangential velocities, an aspect also inferred by Gañán Calvo & López-Herrera (2021) from their analysis of streamlines of the liquid flow, which actually scale differently since they are based on fluid velocities, while we present interface velocities.

In the present paper we present experimental results concerning the dynamics of cavity collapse of a free-surface bubble. Scaling laws for the duration of collapse, the various velocities of collapse and the volume fluxes involved in the collapse are established. We show that precursory capillary waves reduce the velocity of the moving kink in the tangential and the normal directions. Since the kink movement is a wave propagation velocity, the volume fluxes are shown to be entirely due to shrinkage of the cavity walls in the normal direction, with a direct dependency on the cavity depth Z_c. The observed jet velocity scaling is also retrieved from the scaling of this normal flux. The effects of viscosity and gravity on cavity collapse are quantified using three parameters: the path correction $\mathscr{L}(Bo)$, the wave resistance factor $\mathcal{W}_R(Oh, Bo)$ and the aspect ratio of the cavity $Z_c(Bo)/R$. These aspects of cavity collapse are essential for the understanding of the effects of viscosity and gravity on jetting.

The paper is organised as follows. In § 2 the experimental set-up and conditions are presented. Then, in § 3, different aspects of cavity collapse, namely the tangential kink velocities, the normal interface velocities of the collapsing cavity boundary and the total time of cavity collapse, are discussed. Scaling relations that explain the effect of gravity and viscosity on these quantities are established in this section. In § 4, the volume influxes related with the interface velocities are determined, with concluding discussions presented in § 5.

2. Experimental conditions

The experiments were conducted in two transparent containers of cross-sectional areas of $5 \times 5\,\mathrm{cm}^2$ and $3.5 \times 5\,\mathrm{cm}^2$, filled with various fluids, *viz.*, distilled water, various

glycerol–water mixtures with weight of glycerine of 48 %, 55 %, 68 % and 72 %, (hereinafter referred to as GW48, GW55, GW68 and GW72), ethanol and 2-propanol. Table 1 shows the properties of these fluids. In order to avoid meniscus effects, the containers were filled with the desired liquids up to the brim. Fine capillaries of various sizes, connected to a constant discharge syringe pump, were kept immersed in the working fluid to create bubbles of different, equivalent, spherical radii R. Low discharge rates were maintained, so that the bubbles were in the periodic discharge regime (Oguz & Prosperetti 1993). To prevent variation in bubble sizes from each capillary, the orientations of the capillaries were maintained the same throughout the experiments (Doshi *et al.* 2003). The bubble occupied the centre of the container. We used La Vision ProHS (frame rate $\leq$ 19 000 Hz) and Photron SA4 (frame rate $\leq$ 100 000 Hz) cameras for high-speed imaging of the side views of the dynamics of the cavities. A high-intensity green LED array was used for back lighting. The image acquisition rates met the condition that $t_i < 1/|\,\mathrm{d}U_{abs}/\mathrm{d}s|$, where $t_i = 1/(\text{frame rate})$ and $\mathrm{d}U_{abs}/\mathrm{d}s \approx (U_{abs}(t_2) - U_{abs}(t_1))/(\mathrm{d}(t_2) - \mathrm{d}(t_1))$ is the spatial gradient of the absolute velocity of the kink along the cavity, where U_{abs} are the absolute velocities, and d the linear displacements, of the kink at the two successive times t_1 and t_2. The spatial resolution was such that $\Delta Z_i < U_{abs}\ t_{exp}$, where ΔZ_i is the size of each pixel and t_{exp} is the exposure time. The lowest and the highest resolutions for the imaging were 27 μm pix^{-1} and 3.4 μm pix^{-1}, respectively.

The following length measurements were done by counting the pixels between the appropriate liquid–gas interfaces seen in the images. The equivalent spherical bubble radii (R) were measured from the images of the rising bubbles generated at the capillaries. The cavity shrinking lengths along the equatorial plane D_{ne} and along the vertical plane D_{nb} were measured as a function of time from the instantaneous images of the collapsing cavity. The time t corresponding to each image was estimated from the frame rate of recording, with the zero time being the time of thin film rupture. The total time of cavity collapse t_{bc} was measured by counting the number of images starting from the thin film rupture till the cavity becomes conical (see figure 2*d*). The times corresponding to the lengths D_{ne} and D_{nb} were measured similarly. The bottom diameter of each conical cavity $2r_b$ was measured as the horizontal distance between the kinks seen on either sides of the vertical centre line of the bubble, at the instant of flow convergence $t = t_{bc}$ (see figure 2*d*), beyond which the cavity bottom underwent a significant upward movement (see figure 3*i*,*j*) due to jet formation.

We consider the kink propagation and the precursor capillary waves as two different physical phenomena. The precursory capillary waves act as deformations on the convex bubble cavity boundary (S2), whereas the kink is defined as the intersection of the concave cavity opening (S1) with the convex bubble cavity boundary (S2), independent of the presence or the absence of these precursor capillary waves (see figure 2*a*). Velocities of the moving kink, in directions tangential and normal to the cavity surface (U_t and U_n), were estimated by resolving the absolute velocities of the kink U_{abs} in two mutually orthogonal directions, as shown in figure 2(*c*). The absolute displacements of the kink were measured by finding its coordinates at various instances, with U_{abs} at each instant being obtained by dividing these absolute displacements by the corresponding time gap between the images. The angle γ at each instant (see figure 2*c*) was measured throughout the collapse duration by finding $\tan\gamma$ by vectorial decomposition of the corresponding absolute velocity along the tangential and the normal directions. Polynomial fits of the progressive displacements in the tangential direction (d_t) as a function of time, similar to that shown in the inset (*a*) of figure 5, were used to calculate $U_t(t)$ by taking the time derivative of the fits. The curve fits were carried out for the complete time sequence of d_t

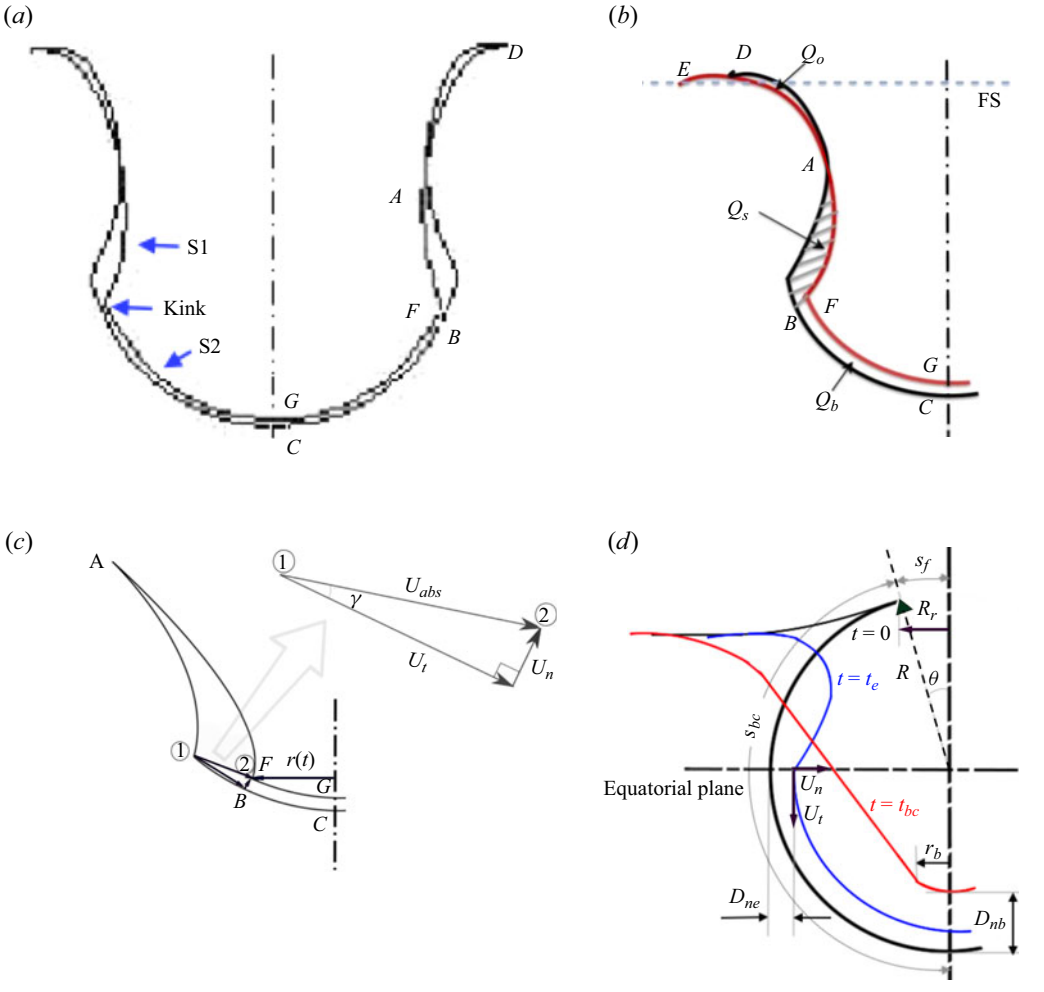

Figure 2. Schematics depicting the parameters and terminologies describing the cavity collapse. (*a*) The actual cavity contours at two time instances, extracted from experiments with a bubble of $R = 0.175$ mm in water showing the kink. S1 and S2 denote the concave and the convex boundaries of the cavity (also see figure 3*e*). (*b*) The side volume flux Q_s and the bottom volume flux Q_b due to the difference between the side and the bottom cavity contours at two successive time instances. Similarly, Q_o is the volume outflux at the top, estimated as the difference between the cavity contours at the free surface, FS. (*c*) Schematic of the collapsing cavity contours at two time instances, with the position of the kink at the different times marked as ① and ②. The absolute, tangential and normal velocities of the kink are shown in the associated vector triangle. (*d*) Schematic of the cavity contours at the following times: (i) $t = 0$ (black); the initial cavity contour when the thin film is ruptured, (ii) $t = t_e$ (blue); the cavity contour when the kink has arrived at the equatorial plane of the cavity (denoted by the horizontal line) showing the equatorial cavity shrinkage D_{ne}, (iii) $t = t_{bc}$ (red); the cavity contour when the kink has arrived at the bottom when the cavity has the form of a smooth funnel with bottom radius r_b and vertical cavity retraction D_{nb}.

and the typical degree of the polynomial fit was 8. The root mean square error for all the curve fits for displacements in our study were extremely small, approximately of the order of 10^{-5} mm, hence, the polynomial fits that we used does not affect the accuracy of the results. In the same way, the normal velocities U_n were estimated from the corresponding progressive normal displacements.

We define three volume fluxes related with the cavity boundary movement: the side (tangential) volume influx Q_s, the bottom (normal) influx Q_b and the side volume outflux Q_o, with the total filling rate being $Q_T = Q_s + Q_b$. The area ABF shown in figure 2(*b*) is the area swept by two successive positions of the kink as it travels along the cavity surface and inwards, with the corresponding side (tangential) volume influx being Q_s. Similarly, the area BCGF is the area swept by the normal motion of the bottom regions of the cavity, with corresponding volume influx being Q_b. The volume outflux Q_o, corresponding to the area DA, was only measured for a single bubble since it was time invariant and hence was not a dynamic quantity. All the volumes were measured as follows: the edges of the collapsing cavity were extracted from images using Canny or Sobel edge detection criteria, depending on the noise levels in the image sequence. Two successive contours were superimposed to produce a sequence of edge pairs (see figure 2*a*) with time. Within two successive contours, the radial distance (r_p) of each pixel and the total number of pixels η_p were measured at each time. The volume contributed by a square pixel inside the two edges, $2\pi r_p \Delta Z_i{}^2$, was estimated. This process was repeated for all the pixels inside the contours, and the volume contributions from each pixel were added. The value of this cumulative volume was then divided by the time gap between the two frames to find the volume flux. The same method was continued for the entire sequence of contour pairs to obtain the volume fluxes as a function of time.

3. Cavity collapse

Figure 3 shows a sequence of the stages of the collapse of a bubble at the free surface for a low-viscosity fluid (water, $Oh = 0.0055$). The corresponding stages for a high-viscosity fluid (GW55, $Oh = 0.034$) are shown in figure 4. In both cases, an axisymmetric kink (figure 3*e*) is seen travelling from the cavity top to the bottom-most part of the cavity, where the cavity boundary converges. For the low-viscosity case (figure 3), precursor capillary waves (see *B* in figure 3*h*) are seen moving ahead of the main (kink) wave. We observe these capillary waves throughout the collapse, only when $Oh < 0.02$, as it is the case in figure 3, resulting in a sharp front edge of the kink, as can be seen in figure 3. When $Oh > 0.02$, as shown in figure 4, these precursory capillary waves are fully damped by the viscous effects before they reach the cavity bottom, resulting in a more rounded front edge of the kink. As can be seen from figures 3 and 4, the kink travels along the cavity surface, while the cavity itself is shrinking normal to its surface. Thus, at any instant, the kink has velocities tangential and normal to the cavity surface, up to the flow convergence at the cavity bottom. It is noteworthy to mention that only the radial interface velocity is equal to the fluid velocity. We analyse these velocities in detail in the following sections.

3.1. *Tangential wave propagation velocity of the kink*

The tangential wave propagation velocity U_t of the kink (herein after simply the tangential velocity) has been measured as discussed in § 2. Inset (*b*) in figure 5 shows the variation of the dimensionless tangential velocity (U_t/U_c) with the dimensionless time (t/t_c), where $t_c = \sqrt{\rho R^3/\sigma}$ is the capillary time scale, for bubbles of similar *Bo* in GW72, $Oh = 0.0427$ (red circle), and in water, $Oh = 0.0028$ (yellow square). The value of U_t is observed to be constant, except at the beginning and the end of the collapse, and scales with the capillary velocity $U_c = \sqrt{\sigma/\rho R}$, in a way similar to the observations of Krishnan & Puthenveettil (2015), Krishnan *et al.* (2017) and Gordillo & Rodríguez-Rodríguez (2019). However, for $Oh = 0.0028$, where precursor capillary waves occur ahead of the main kink wave, as shown in figure 3, the values of U_t/U_c are around 40 % lower compared with those at

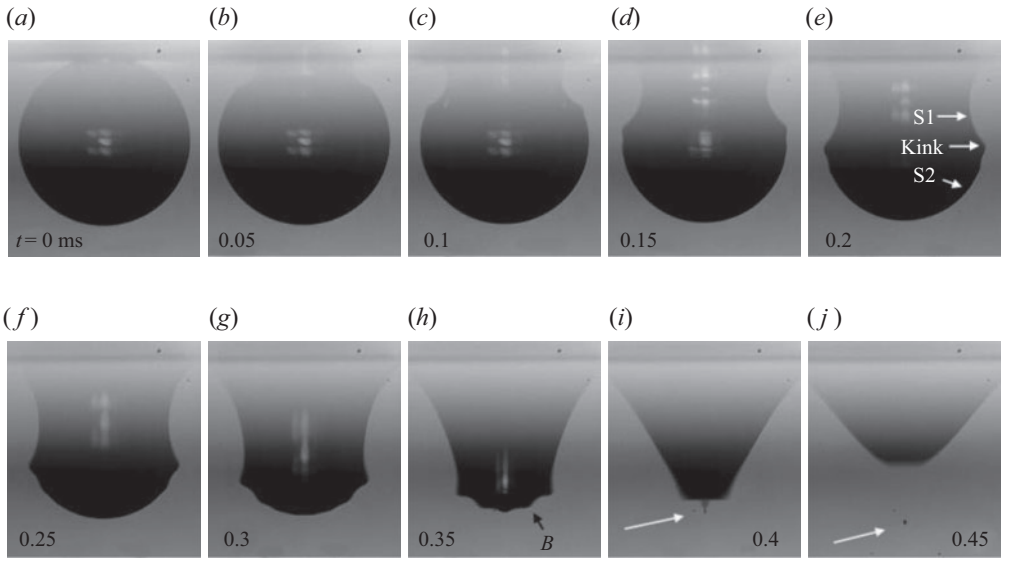

Figure 3. Image sequence showing the stages of cavity collapse in a low-viscosity fluid, showing the presence of precursory capillary waves. The bubble is of radius $R = 0.47$ mm in water ($Bo = 0.03$, $Oh = 0.0055$). Bubble pinch-off from wave focusing, creating a downward gas jet of radius 8.6 µm, is also seen in (*h–i*). The width of each image is 0.97 mm. Movie 1 is available at https://doi.org/10.1017/jfm.2024.26.

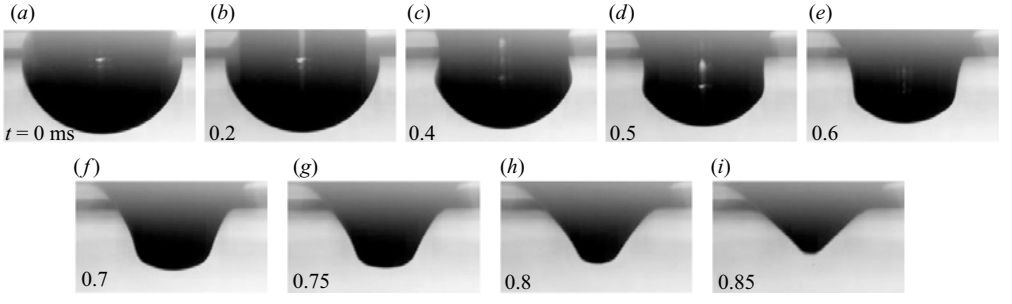

Figure 4. Image sequence showing the stages of cavity collapse due to a $R = 0.7$ mm bubble ($Bo = 0.08$) in a high-viscosity fluid (GW55, $Oh = 0.034$) that is relatively free of the precursory capillary waves. The image width is 1.7 mm. See movie 2.

$Oh = 0.0427$, where the precursor capillary waves are fully damped (figure 4). We observe this behaviour with all the bubbles when $Oh < 0.02$. Similar decreasing velocity of the kink in the presence of precursor capillary waves is clearly seen in the velocity data of Ji, Yang & Feng (2021) (see Ji *et al.* 2021, figure 5) for the bursting of bubbles in oil covered water surface, where the oil layer covering the kink enhances the damping of precursor capillary waves. Thus the capillary velocity scale alone does not collapse the tangential velocity data for different viscosity fluids, possibly due to the effect of precursor capillary waves on U_t. A new scaling relation for U_t is therefore needed to account for the effect of viscous damping of the precursor capillary waves, and a possible (weak) gravity effect. Using an energy balance at the kink, we now obtain such a scaling relation that collapses the tangential velocity data.

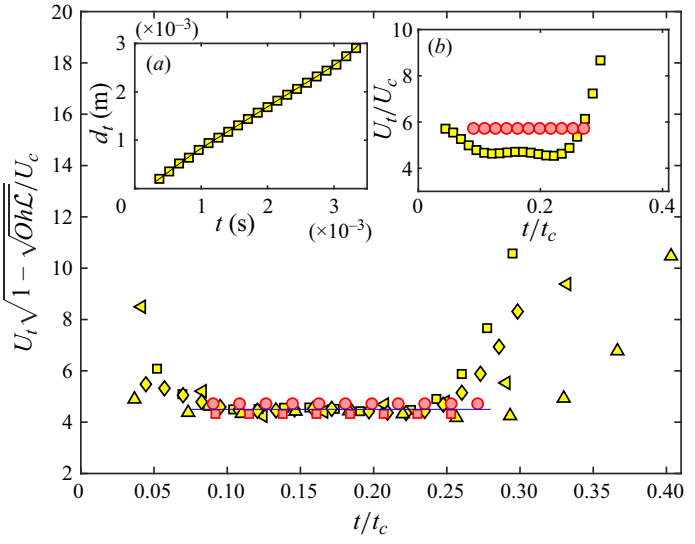

Figure 5. Normalised tangential velocity of the kink, accounting for the wave resistance of precursory capillary waves, $\mathcal{W}_R(Oh, Bo)$, and the path correction due to gravity effects, $\mathcal{L}(Bo)$, as in (3.13), plotted as a function of the dimensionless time t/t_c, for bubbles of $0.001 < Bo < 1$ and $0.001 < Oh < 0.05$. Symbols: ▲, yellow, $R = 0.175$ mm ($Bo = 4.2 \times 10^{-3}$, $Oh = 0.0099$); ◀, yellow, $R = 0.47$ mm ($Bo = 3 \times 10^{-2}$, $Oh = 0.0055$); ■, yellow, $R = 1.74$ mm ($Bo = 4.1 \times 10^{-1}$, $Oh = 0.0028$) and ♦, yellow, $R = 2.15$ mm ($Bo = 6.3 \times 10^{-1}$, $Oh = 0.00255$). Aforementioned data are from water. Data with GW72 are: ■, red, $R = 1.59$ mm ($Bo = 4.8 \times 10^{-1}$, $Oh = 0.0481$); •, red, $R = 2.02$ mm ($Bo = 7.7 \times 10^{-1}$, $Oh = 0.0427$). —, $U_t\sqrt{1-\sqrt{Oh}\mathcal{L}}/U_c = 4.5$. In inset ($a$), the cumulative distance, d_t, travelled by the kink in the tangential direction is plotted versus time for a bubble of $R = 2.14$ mm in water, with — the polynomial fit used for calculating U_t. The inset (b) shows the offset between the dimensionless tangential velocities of the kink in water and GW72, when precursory capillary wave effects are not taken into account.

3.1.1. *Energy balance at the kink*

The retraction of the rim right after the film rupture provides the kinetic energy associated with the kink movement. Since the kink moves with constant velocity U_t, as seen in § 3.1 and figure 5, we assume a steady state balance of the energy of the kink movement. Consider the area corresponding to the side flux AFB as shown in figure 2(a), with $2\pi R$ and R being the characteristic lengths along azimuthal and vertical directions, respectively. The characteristic volume of the kink then scales as $2\pi R^2\beta$, with β being the length scale of the kink, where the velocity is the tangential velocity U_t. Note that the kink is identified as a small region (the intersection of S1 and S2 as shown in figure 2a) where the characteristic velocity is U_t, and the movement of the surface above the kink of lesser velocities is neglected. We assume that β is directly related to the amplitude of the precursory capillary wave $\beta \simeq a$. Hence, the characteristic volume of the kink is $2\pi R^2 a$, and the corresponding kinetic energy is $KE = (1/2)\rho 2\pi a R^2 U_t^2$.

The precursory capillary waves are driven by the sudden movement of the kink. Consequently, a part of the kinetic energy of the kink is utilised for the creation of these waves (KE_{loss}) and a part of the kinetic energy is converted to surface energy SE (i.e. due to the creation of the kink area), where $2\pi R$ and a are the characteristic lengths along azimuthal and vertical directions, respectively, of the precursory capillary wave. Since the motion is felt over a length scale of wavelength λ, the characteristics volume of the precursory capillary wave for one cycle is chosen as $2\pi Ra\lambda$. The corresponding kinetic

energy is $KE_{loss} = (1/2)\rho a 2\pi R\lambda U_t^2$, as these waves move with the same velocity that of the kink.

The surface energy corresponding to the creation of the kink area is $SE = \sigma 2\pi Ra$, where σ is the surface tension. Balancing the energy terms $KE = KE_{loss} + SE$, gives

$$\frac{1}{2}\rho a R^2 {U_t}^2 = \alpha_1 \frac{1}{2}\rho a R\lambda {U_t}^2 + \alpha_2 \sigma a R, \tag{3.1}$$

where α_1, α_2 are constant prefactors. Rearranging (3.1), we obtain the Weber number of cavity collapse in the form

$$We_c = \frac{\rho {U_t}^2 R}{\sigma} = \left(\frac{U_t}{U_c}\right)^2 = \frac{2\alpha_2}{1 - \alpha_1 \lambda/R}. \tag{3.2}$$

The expression (3.2) quantifies the reduction in U_t/U_c, shown in the inset (*b*) of figure 5, due to the presence of precursory capillary waves. The dimensionless wavelength λ/R of the dominant precursory capillary wave in (3.2) depends on the total time of cavity collapse, which, as we show later in § 3.1.3, depends on Oh and Bo. Then, (3.2) can be written as

$$U_t = \alpha_3 U_c \mathcal{W}_R(Oh, Bo), \tag{3.3}$$

where $\alpha_3 = \sqrt{2\alpha_2}$ and

$$\mathcal{W}_R(Oh, Bo) = 1/\sqrt{1 - \alpha_1 \lambda/R}, \tag{3.4}$$

is the wave resistance factor that accounts for the reduction in U_t due to the precursory capillary waves. Here, $\mathcal{W}_R(Oh, Bo)$ depends on λ/R, which in turn depends on the total time of cavity collapse, t_{bc}, since viscous damping during t_{bc} affects λ/R. The above analysis did not consider the overall complexities of the flow, especially in the region away from the interface. However, with the use of appropriate prefactors, as we show later, (3.3) does capture the kinematics of the kink motion along the tangential direction. We now discuss the dependency of t_{bc} on Oh and Bo, which allows us to get the dependency of λ/R on Oh and Bo, and thereby, an expression for $\mathcal{W}_R(Oh, Bo)$.

3.1.2. *Total time of cavity collapse t_{bc}*

Since the time taken for the disintegration of the thin film at the top of the bubble is negligible (Duchemin *et al.* 2002), we consider the time at which the retracting rim has reached the outer edge of the film, at R_r (see figure 2*d*), to be the reference time $t = 0$. The time from $t = 0$ to the stage where the cavity has become conical, just before jet initiation (figure 3*i*), is measured as the total time of cavity collapse, t_{bc}. In figure 6, t_{bc}, normalised by the capillary time scale $t_c = \sqrt{\rho R^3/\sigma}$, is plotted as a function of Bo. The experimental data indicate a gravity dependency of t_{bc}/t_c in the form

$$\frac{t_{bc}}{t_c} = 0.26 Bo^{-0.1}. \tag{3.5}$$

This Bond number dependence of t_{bc} can be physically explained by evaluating the time taken by the kink to travel along the cavity boundary. The length of the path travelled by the kink (s_{bc}) along the cavity surface, from the rim till the bottom of the cavity (see figure 2*d*), is a function of Bo because the static shape of the free-surface bubble depends on Bo. For $Bo \leq 1$

$$s_{bc} = (\pi R - s_f) Oh^n \approx (\pi R - R_r) Oh^n, \tag{3.6}$$

where $s_f = R\theta$ (see figure 2*d*), with $\theta = R_r/R$ for small θ and R_r is the rim radius (see figure 1*a*), which is a function of Bo (Puthenveettil *et al.* 2018). The factor Oh^n, where

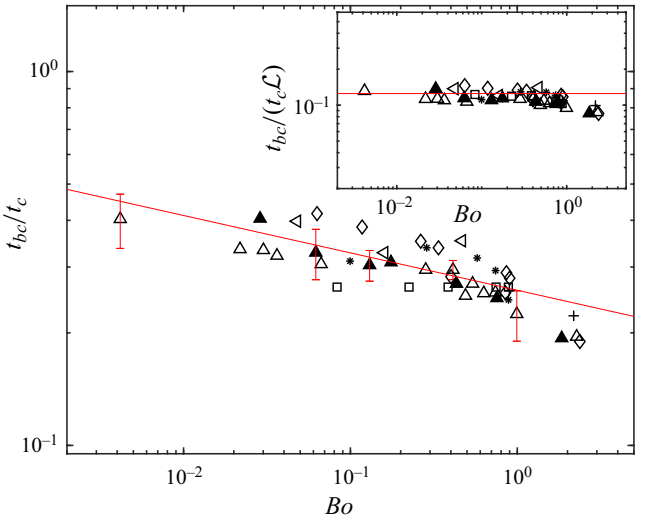

Figure 6. The effect of Bond number on the dimensionless total time of cavity collapse t_{bc}/t_c, where t_c is the capillary time scale. —, $t_{bc}/t_c = 0.26Bo^{-0.1}$. In the inset, the dimensionless total time of cavity collapse, accounting for the path correction due to gravity, $t_{bc}/(t_c\mathscr{L})$, is plotted as a function of Bo. —, $t_{bc}/(t_c\mathscr{L}) = 0.13$ (3.10). △, water; ◁, ethanol; ▲, GW48 (30 °C); ∗, GW68; ◇, GW72; +, 2-propanol; □, GW55.

n is a positive exponent, appears in (3.6) because the bottom radius of the conical cavity r_b at the time $t = t_{bc}$ (see figure 2*d*) depends on Oh (see figure 14). This dependence of r_b on Oh arises since the occurrence of capillary waves, which increase r_b (Gordillo & Rodríguez-Rodríguez 2019), depends on Oh. After substituting s_{bc} from (3.6) in $t_{bc} \approx s_{bc}/U_t$, with U_t given by (3.3), we obtain

$$t_{bc} \approx \frac{1}{\alpha_3} t_c \mathscr{L} \zeta, \tag{3.7}$$

where $\zeta = Oh^n/\mathcal{W}_R$, with $\mathcal{W}_R$ given by (3.4) and

$$\mathscr{L}(Bo) = \pi - R_r/R \tag{3.8}$$

is the path correction term that accounts for the gravity dependence of the path length s_{bc} travelled by the kink. In (3.8), the dimensionless rim radius

$$R_r/R = \sqrt{4/3 - 2(1/Bo + 1/Bo^2) + \sqrt{-4/3Bo^2 + 8/Bo^3 + 4/Bo^4}}, \tag{3.9}$$

when $Bo \leq 1$ (Puthenveettil *et al.* 2018).

Equation (3.7) delineates the capillary effects on the total time of cavity collapse through t_c, while the gravity and the viscous effects enter through $\mathscr{L}(Bo)$ and ζ, respectively. The inset in figure 6 shows that the measured values of $t_{bc}/(t_c\mathscr{L})$ collapse onto

$$t_{bc} \approx 0.13 t_c \mathscr{L}, \tag{3.10}$$

for bubbles of various diameters with $0.001 < Bo < 1$ and fluids of various viscosity with $0.001 < Oh < 0.1$. The deviation of the data from (3.10), when $Bo > 1$, occurs because s_{bc} starts to deviate from (3.6) and R_r/R from (3.9) due to increasing deviations of the shape of the cavity from that of a truncated sphere. Equations (3.7) and (3.10) imply that $Oh^n/(\alpha_3\mathcal{W}_R) = 0.13$ for the present range of $0.001 < Bo < 1$ and $0.001 < Oh < 0.1$.

Then, the increase in s_{bc} at larger Oh due to decreasing r_b (see (3.6) and figure 14) seems to be offset by increasing velocities due to increased damping of precursory capillary waves (see (3.2)), so that t_{bc} becomes independent of Oh, as given by (3.10). The total time of cavity collapse then follows a capillary time scale t_c, modified by the term $\mathscr{L}$, which depends on Bo through (3.8) and (3.9), with negligible dependence on viscosity.

3.1.3. *Wavelength of precursor capillary waves and scaling of U_t*

The Bo dependence of t_{bc} given by (3.10) necessitates the modification of the wave damping scaling relation $\lambda/R \propto \sqrt{Oh}$ presented in Krishnan *et al.* (2017), which was based on $t_{bc} \approx 0.3t_c$, proposed by Krishnan & Puthenveettil (2015). It has been shown that the amplitudes of the capillary waves fall off exponentially in the form $a/a_0 = e^{-\kappa t}$, where a_0 and a are, respectively, an initial and a later wave amplitude, with $\kappa = 8\pi^2\mu/\rho\lambda^2$ being the wave damping coefficient (Lighthill 1978). The waves can be considered fully damped at the end of the cavity collapse time t_{bc}, when

$$\kappa t_{bc} = \frac{8\pi^2\mu t_{bc}}{\rho\lambda^2} = 4, \tag{3.11}$$

as presented in Krishnan *et al.* (2017). Substituting (3.10) for t_{bc} in (3.11) and rearranging, we obtain the dimensionless wavelength that is damped in the time t_{bc} as

$$\frac{\lambda}{R} = c_2\sqrt{Oh\mathscr{L}}, \tag{3.12}$$

where $c_2 = 0.5\pi$. The relation (3.12) gives the largest damped wavelength at the bottom of the cavity for a given Oh and Bo. It also predicts the Oh at which a given wavelength will be damped at the bottom of the cavity for a specified Bo. For example, the experimental values corresponding to $Bo \approx 0.37$ are typically $\lambda/R \approx 0.4$, which, according to (3.12), when $\mathscr{L} \approx 2.5$, requires $Oh \approx 0.02$, the value below which precursory capillary waves are observed at the cavity bottom. Precursory capillary waves are formed at all Oh. These precursory capillary waves impart wave resistance to the moving kink before they are fully damped. However, the spatial location ahead of the kink at which the precursory capillary waves are fully damped depends on the value of Oh. Since $\lambda/R \simeq 0.4$, when $Oh \simeq 0.03$ precursor capillary waves are damped before arrival of the kink at the cavity bottom when $Oh \geq 0.03$. Practically, no precursor waves exist when $Oh \geq 0.04$.

The gravity dependency of the path correction $\mathscr{L}$ is given by (3.8) and (3.9). Since R_r/R increases with increasing Bo, as given by (3.9), $\mathscr{L}$ decreases when Bo is increased. Thus, when Bo is large, Oh needs to be larger for the waves to be damped in the time t_{bc}.

Substituting λ/R from (3.12) in (3.3) and rearranging, we get

$$U_t \approx \frac{\alpha_3 U_c}{\sqrt{1 - c_2\alpha_1\sqrt{Oh\mathscr{L}}}}. \tag{3.13}$$

In figure 5, the dimensionless tangential velocity $U_t\sqrt{1 - c_2\alpha_1\sqrt{Oh\mathscr{L}}}/U_c$ is plotted against the dimensionless time t/t_c for bubbles in water (yellow symbols) and GW72 (red symbols) in the range $2 \times 10^{-3} < Bo < 1$ and $0.001 < Oh < 0.05$, with the upper value

of Oh being somewhat larger than 0.03 obtained above from (3.12). The data collapse onto

$$\frac{U_t\sqrt{1-\sqrt{Oh\mathscr{L}}}}{U_c} = 4.5, \tag{3.14}$$

for $0.05 < t/t_c < 0.3$, the uniform phase of tangential motion, implying that $\alpha_1 = 1/c_2$ and $\alpha_3 = 4.5$. In the limit $Oh \to 0$, the relation (3.14) matches with the relation for the absolute velocity (see figure 2*c*) of the dominant capillary wave, $U_{abs} \simeq 5U_c$, proposed by Gordillo & Rodríguez-Rodríguez (2019), based on their numerical simulation in the vanishing Bond number limit $Bo \ll 0.1$. At finite Bo and Oh, (3.14) captures the complex dependence of the kink velocity on Oh and Bo that occurs through the damping of the precursory capillary waves.

Comparing (3.14) with (3.3), shows that the wave resistance factor in (3.3) is of the form

$$\mathcal{W}_R(Oh, Bo) = \frac{1}{\sqrt{1-\sqrt{Oh\mathscr{L}}}}. \tag{3.15}$$

Then, the final scaling of the tangential velocity of the kink is $U_t \approx 4.5U_c\mathcal{W}_R$, where $\mathcal{W}_R$ is given by (3.15).

The constancy of U_t with respect to time, seen in figure 5, could also be understood in terms of the phase velocity of the precursory capillary waves. The kink produces a wave disturbance, of wavelength λ, at the cavity surface, which propagates like a capillary wave with a phase velocity $c_p = (2\pi)^{1/2}\sqrt{\sigma/\rho\lambda}$. Substituting λ from (3.12) in this relation gives

$$c_p = 2.8U_c(Oh\mathscr{L})^{-1/4}, \tag{3.16}$$

which is close to (3.14), although the dependency on viscosity and gravity shown by (3.14) is not fully captured by c_p. However, the important point is that the phase velocity of the precursory capillary wave does give an argument for U_t being constant in time, as seen in figure 5.

3.2. *Shrinking of the cavity boundary in the normal direction*

In figure 7(*a*) the initial cavity boundary (the bubble boundary) at $t = 0$ is compared with that at a later instant ($t = 0.15$ ms) for a bubble of $R = 0.5$ mm in water. The cavity contours clearly indicate the retraction of the cavity in the normal direction everywhere below the kink rim, as indicated by the arrows. This cavity shrinkage is due to the sudden reduction of the gas pressure in the cavity after rupture of the surface film, leading to an imbalance with the surface tension force, which scales as σ/R.

In figure 7(*b*,*c*), the trajectories of the kink are indicated by the continuous (red) lines in the images of a bubble of $R = 2.15$ mm in water and of a bubble of $R = 2$ mm in GW72, respectively. It is seen that the extent of shrinkage, i.e. the gap between the initial cavity contour and the red line, is larger for the bubble in the viscous fluid GW72 than it is in water. It is also seen that in the water bubble in figure 7(*b*) that the kink undergoes a sudden jump towards the end, while the trajectory of the kink in GW72 (figure 7*c*) is smooth throughout the collapse. A corresponding rise in the normal velocity of the kink in bubbles in water towards the end of the collapse is seen in figure 8, which shows the velocity of the kink in the direction normal to the cavity boundary, U_n, normalised with the capillary velocity, U_c, plotted as a function of the dimensionless time t/t_c. The velocity data also show a slow increase with time, indicating a weak acceleration, except in water, where toward flow convergence, U_n/U_c values increase abruptly due to the presence of

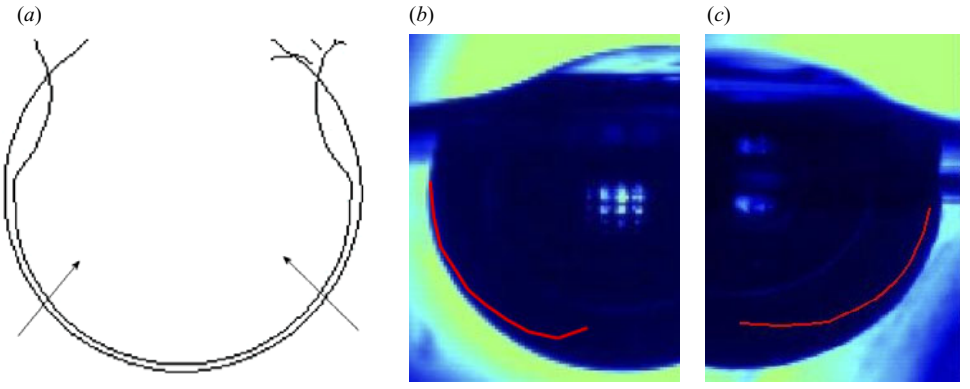

Figure 7. Shrinking of the cavity in the normal direction. (*a*) Contours of the cavity at two time instances, $t = 0$ ms and $t = 0.15$ ms, superimposed for a bubble of $R = 0.5$ mm in water. Arrows show the shrinking of the cavity boundary below the kink rim. The (red) lines superimposed over the static shapes of the bubbles in (*b*,*c*) indicate the trajectories of the kinks extracted from their cavity collapse. The bubbles in (*b*,*c*) are of similar size but differ significantly in *Oh*; (*b*) $R = 2.15$ mm, $Bo = 0.63$, $Oh = 0.00255$ in water; (*c*) $R = 2$ mm, $Bo = 0.77$, and $Oh = 0.0427$ in GW72. The widths of the images are 5.43 mm and 2.85 mm.

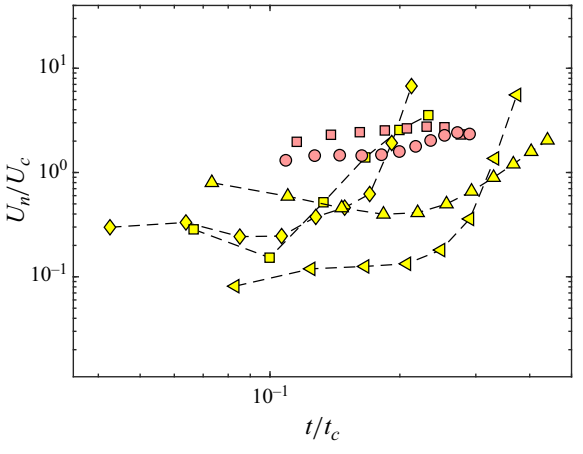

Figure 8. The dimensionless normal velocity of the leading edge U_n/U_c as a function of the dimensionless time t/t_c. The symbols are the same as those in figure 5, namely: ▲, yellow, $R = 0.175$ mm ($Bo = 4.2 \times 10^{-3}$, $Oh = 0.0099$); ◀, yellow, $R = 0.47$ mm ($Bo = 3 \times 10^{-2}$, $Oh = 0.0055$); ■, yellow, $R = 1.74$ mm ($Bo = 4.1 \times 10^{-1}$, $Oh = 0.0028$) and ♦, yellow $R = 2.14$ mm ($Bo = 6.3 \times 10^{-1}$, $Oh = 0.00255$). Aforementioned data are from water. Data with GW72 are: ■, red $R = 1.59$ mm ($Bo = 4.8 \times 10^{-1}$, $Oh = 0.0481$); ●, red $R = 2.02$ mm ($Bo = 7.7 \times 10^{-1}$, $Oh = 0.0427$).

precursory waves, discussed in § 3.1. This sudden rise in velocity of the kink, by an order of magnitude, is a feature observed for bubbles in low-viscosity fluids of $Oh < 0.02$, where precursory capillary waves are present. We show in Appendix B that the higher values of the normal velocity towards the end of the cavity collapse is of the order of the velocity scale $2\sqrt{\sigma/\rho\lambda}$. Figure 8 shows that the scaled normal velocities of the kink in the viscous fluid (GW72, $Oh > 0.02$) are higher than those in water ($Oh < 0.02$); clearly, a capillary velocity scaling alone, as in the figure, does not collapse the normal velocities.

It needs to be noted that a $\mathcal{W}_R$ correction of U_n/U_c, as applied to the dimensionless tangential velocity U_t/U_c earlier (see (3.3)) to account for the precursor capillary wave

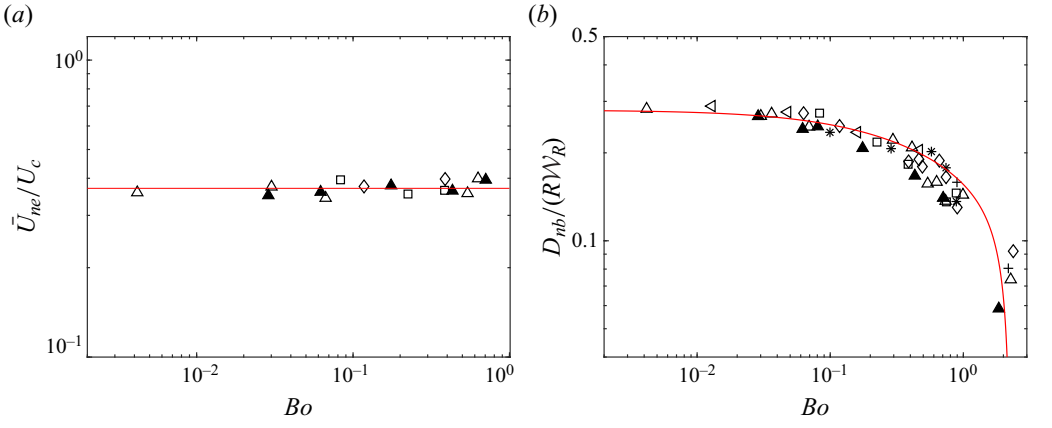

Figure 9. (*a*) Variation of the dimensionless average shrinkage velocity at the equatorial plane ($\bar{U}_{ne}/U_c$) with *Bo*. — , $\bar{U}_{ne}/U_c = 0.37$. (*b*) Dimensionless shrinkage of the cavity bottom, $D_{nb}/(R\mathcal{W}_R)$, plotted as a function of *Bo*. —, $D_{nb}/(R\mathcal{W}_R) = 0.14(Z_c/R)$. △, water; ▲, GW48 (30 °C); □, GW55; ∗, GW68; ◇, GW72; +, 2-propanol; ◁, ethanol.

effects, does not collapse the normal velocity data. To address this scaling problem, we now analyse the average velocity of shrinkage of the cavity in two mutually perpendicular directions, *viz.*, (i) in the equatorial plane in the horizontal direction, where the local radius of the cavity from its vertical axis of symmetry is maximum, and (ii) in the meridional plane along the vertical axis of symmetry (see figure 2*d*).

3.2.1. *Average normal shrinkage velocity in the equatorial plane and along the vertical axis*

Figure 9(*a*) shows the average shrinkage velocity normal to the cavity boundary in the equatorial plane $\bar{U}_{ne} = D_{ne}/t_e$, scaled with the capillary velocity scale, as a function of *Bo*. Here, D_{ne} is the average normal displacement of the cavity surface in the equatorial plane over a time t_e, where t_e is the time taken for the kink to reach the equatorial plane; these are shown in figure 2(*d*). It is seen in figure 9(*a*) that $\bar{U}_{ne}/U_c$ is independent of *Bo* and scales as

$$\bar{U}_{ne} = 0.35U_c. \tag{3.17}$$

Thus, in the equatorial plane, where there is symmetry in the azimuthal direction, the velocity of shrinking scales with the capillary velocity U_c, devoid of any viscous and gravity effects.

On the contrary, the normal shrinkage at the cavity bottom is strongly dependent on *Bo*, as is seen in figure 9(*b*), where the dimensionless normal distance of shrinking at the bottom of the cavity D_{nb}/R over a time t_{bc}, corrected by $\mathcal{W}_R$, similar to that in figure 5, is plotted as a function of *Bo*. The variation of the data in the figure is well represented by the variation of the normalised cavity depth Z_c/R with *Bo*, obtained using the closed form solution for Z_c/R in terms of *Bo*, given by Puthenveettil *et al.* (2018) as (C1); this representation reveals the dependence of D_{nb} on Z_c. Thus, the expression of the best fit of the data in figure 9(*b*) is

$$D_{nb}/(R\mathcal{W}_R) = 0.14(Z_c/R). \tag{3.18}$$

The average velocity of cavity shrinking at the bottom is $\bar{U}_{nb} = D_{nb}/t_{bc}$. Using (3.18) and t_{bc} from (3.10), the average vertical shrinking rate of the cavity bottom then becomes

$$\frac{\bar{U}_{nb}}{U_c} = \frac{Z_c}{R}\frac{\mathcal{W}_R}{\mathscr{L}}, \tag{3.19}$$

where Z_c/R is the static aspect ratio of the cavity, given by (C1). Equation (3.19) shows that the precursory capillary waves act as deformations on the cavity surface, reducing cavity shrinking velocity at the bottom of the cavity, when $Oh < 0.02$. This reduced shrinking velocity of the cavity in low-viscosity fluids can also be seen in figure 8. The resulting capillary velocity scaling of $\bar{U}_{nb}$ is in agreement with the radial velocity scaling of the cavity in the inviscid limit, proposed by Gañán Calvo & López-Herrera (2021) for $Oh \ll 0.04$. However, the present $\bar{U}_{nb}$ differs from the viscous–capillary velocity (V_μ) dependence of radial velocity proposed by Gañán Calvo & López-Herrera (2021), for the final stage of collapse at around $Oh = 0.04$. This difference is possibly due to the fact that $\bar{U}_{nb}$ is the velocity averaged over t_{bc}, which may not capture the sharp changes in velocities near the flow convergence. In fact, a direct comparison of our results (both tangential and normal velocities of the interface) with Gañán Calvo & López-Herrera (2021) is difficult because the scalings presented in Gañán Calvo & López-Herrera (2021) are based on the liquid motion, whereas ours are based on the interface movement.

In any case, it is clear from (3.19) and (3.14) that the bottom interface of the cavity, prior to the flow convergence, closes with two different velocity scales, originating from two different physical mechanisms. As we discuss in Appendix A, the velocities normal to the cavity need to be considered while modelling the jet, so as to correctly balance the mass flux associated with the cavity collapse. We show in § 4 that the mass flux, which is entirely due to the radial shrinking of the cavity with normal velocity U_n, is capillary–gravity dependent, and thus is the reason for the unusual gravity dependence of jet velocity for $Bo > 0.1$, reported earlier (Krishnan *et al.* 2017). It is also of interest to note that the cavity shrinking velocity at the equatorial plane $\bar{U}_{ne}$ (3.17) is independent of Oh. This is in contrast with that of $\bar{U}_{nb}$ (3.19), which has a dependence on viscosity through $\mathcal{W}_R$, the wave resistance factor, due to the presence of precursory capillary waves. This difference is expected to be because the precursory capillary waves affect the cavity collapse only after the kink crosses the equatorial plane. In the final phase of cavity collapse, i.e. at the arrival of the kink at the cavity bottom, the rise in the normal velocity in low-viscosity fluids is almost an order of magnitude higher (see figure 8) than that in fluids of high viscosity. This rise in U_n occurs when the capillary waves converge at the cavity bottom (see Appendix B).

Finally, to demonstrate the overall shrinking of the cavity, irrespective of the tangentially moving kink, a free-surface bubble of radius $R = 1.7$ mm was produced in a highly viscous fluid (GW89; $Oh = 0.52$). Since the retraction of the rim is fully damped for $Oh > 0.24$ (see Krishnan *et al.* 2020), we expect the rim retraction, and consequently the kink, to be fully suppressed in this case. Figure 10 shows an image sequence of such a clean spherical shrinking of the cavity surface in the absence of a kink (or tangential movement). This image sequence gives an additional confirmation for the existence of two independent interface dynamics associated with free-surface bubble collapse, *viz.* (i) a tangential wave propagation velocity of the kink driven by the retraction of the rim, and (ii) an overall spherical shrinking of the bubble cavity due to the sudden reduction of gas pressure.

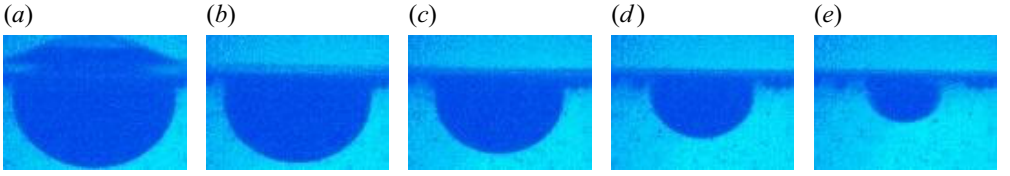

Figure 10. Collapse of a bubble of radius $R = 1.7$ mm ($Bo = 0.54$) in a high viscous fluid (GW89, $Oh = 0.52$). The times corresponding to each image are $t = 0$, 2, 3.25, 4.75 and 6 ms. Width of each image is 3.84 mm.

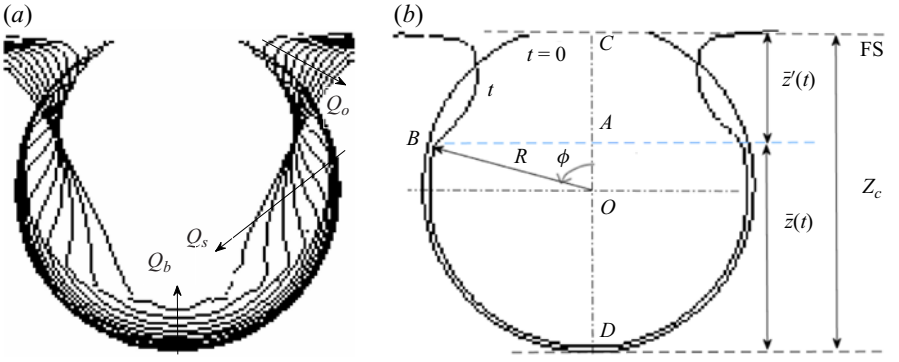

Figure 11. (*a*) Superimposed contours of collapsing cavity at different time instances of bubble $R = 0.175$ mm in water, starting from the static shape at $t = 0$ until the conical cavity shape is reached. The successive contours are separated by 10 μs. See movie 3. (*b*) Contours of initial static cavity configuration, at $t = 0$, and at a later time $t > 0$. The figure shows the various parameters related with the moving kink; the free surface is indicated by FS.

4. The cavity filling rate

Three volume fluxes can be identified in relation with the movement of the cavity boundary, as indicated in figure 2(*b*), and measured, as discussed in § 2. Figure 11(*a*) shows the contours of the collapsing cavity of a bubble of radius $R = 0.175$ mm in water, at different time instances, starting from the static shape of the cavity at $t = 0$ until a conical shape is reached. The volume fluxes that can be identified from the figure, and marked by arrows in the figure, are (i) the side (tangential) volume influx Q_s, (ii) the bottom (normal) influx Q_b and (iii) the side volume outflux Q_o, with the total filling rate being $Q_T = Q_s + Q_b$. Figure 12 shows the variation of the side volume influx Q_s (denoted by hollow symbols) and the total volume influx Q_T (solid symbols) as a function of time, for different size bubbles, in water and GW48. The horizontal and vertical axes in figure 12 span three orders of magnitude of time and volume flux, respectively. The difference between Q_T and Q_s in figure 12 corresponds to the bottom influx Q_b at any given time. The inset in figure 12 shows the variation of the volume outflux Q_o with time, measured for a bubble of radius $R = 0.175$ mm in water. The volume outflux Q_o is not entirely negligible. However, since it is practically constant in time and since Q_T is constant, $Q_T - Q_o$ is also a constant so that the volume expansion of the cavity at the free surface (Q_o) will not change the functional behaviour of Q_T with time. Therefore, Q_o is not considered further in our analysis. As expected, all the volume fluxes increase with increase in bubble size.

Each data set of Q_T shows an approximately constant value with time, indicated by a horizontal dashed line, and then suddenly drops off when $t > t_{bc}$. This sudden change in Q_T is indicative of an unaccounted volume outflux, due to the creation of the jet

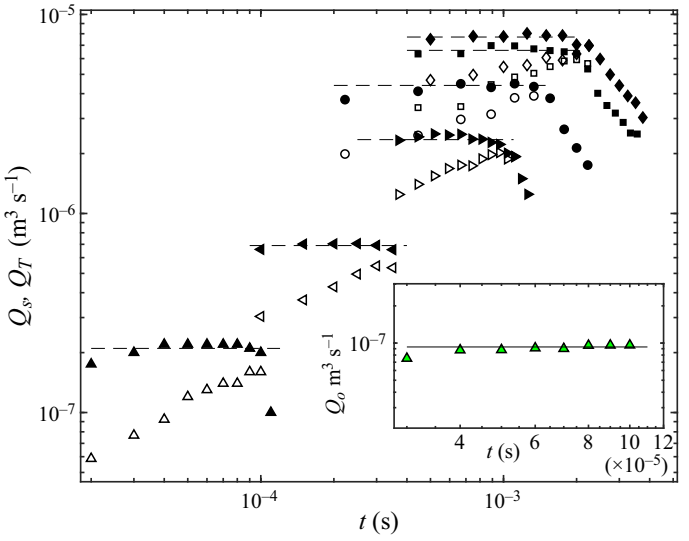

Figure 12. The rate of filling of the cavity from the tangential direction, Q_s (hollow symbols), and the total filling rate Q_T (solid symbols) as functions of time, for bubbles of different Bo and Oh. ♢, $R = 2.15$ mm ($Bo = 0.63$, $Oh = 0.00255$); □, $R = 1.89$ mm ($Bo = 0.49$, $Oh = 0.0027$); ◯, $R = 1.47$ mm ($Bo = 0.3$, $Oh = 0.0031$); ◁, $R = 0.47$ mm ($Bo = 0.03$, $Oh = 0.0055$); △, $R = 0.175$ mm ($Bo = 0.0042$, $Oh = 0.0099$) (all data in water). ▷, $R = 1.04$ mm ($Bo = 0.17$, $Oh = 0.0139$) in GW48. The volume outflux, Q_o, measured for $R = 0.175$ mm in water, is shown in the inset.

inside of the cavity, coinciding with the conical cavity shape. Recently, Gordillo & Blanco-Rodríguez (2023) numerically estimated the radial flow rate per unit length of the cavity and observed that this liquid flow rate remains approximately constant for a very short time duration immediately after $t = t_{bc}$, due to liquid inertia and mass conservation during the short duration after jet initiation. Even though we measure the rates of changes of the cavity boundary volumes, which cannot be directly connected to the flow rates of the liquid outside the cavity, the approximately constant slope of Q_T vs t after jet initiation could be related to such a constant radial liquid flow rate; these need to be investigated in future.

The side volume flux Q_s, which is initially a small fraction of Q_T, increases with time and represents nearly the total volume flux when the cavity becomes a cone. We now obtain a scaling for this Q_s as follows. The characteristic area of the side flux is $2\pi R\bar{z}'(t)$, where $\bar{z}'(t)$ is the height above the kink up to the free-surface level (see figure 11*b*), with the velocity being the tangential velocity of the kink U_t (§ 3.1). Although the kink moves with a velocity U_t, the upper interior region of the concave boundary lags behind the kink (see *A* in figure 2*c*), as the velocity of the interior fluid and the velocity of the interface need not be the same, an aspect clarified in §§ 1 and 3. Such a velocity difference inside the side boundary implies the existence of a shear region, which needs to be accounted for in the side volume flux. Hence, we include a viscous correction term of the form Oh^d to estimate the side flux as $Q_s \sim 2\pi R U_t Oh^d \bar{z}'(t) \sim 2\pi R U_t Oh^d (R - R\cos\phi)$, which then yields

$$\frac{Q_s}{\pi R^2 U_t Oh^d} \approx a_0 + a_1 \sin^2(\phi/2), \tag{4.1}$$

where a_0 and a_1 are constants to be determined from the experiments. In (4.1) $\phi = \omega t + \phi_0$ is the phase angle of the moving kink (see figure 11*b*), where ω is the circular frequency

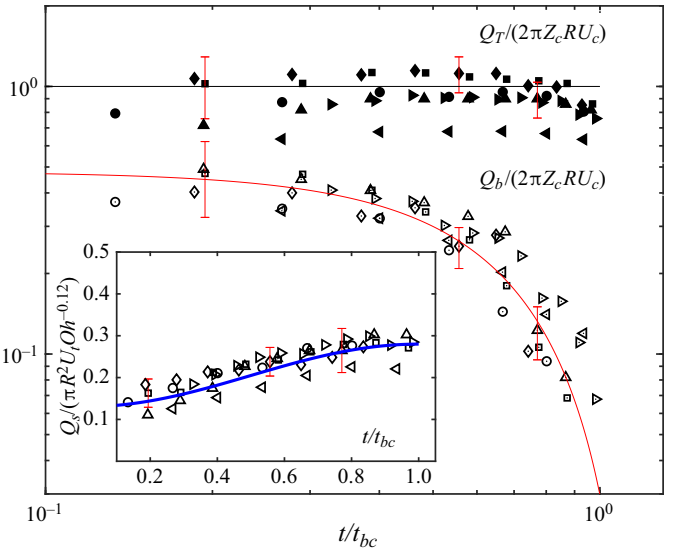

Figure 13. Variation of the dimensionless total volume influx $Q_T/2\pi RZ_cU_c$ and the dimensionless volume influx in the (bottom) normal direction $Q_b/2\pi Z_cRU_c$ as a function of the dimensionless time t/t_{bc}. The inset figure shows the volume influx along the tangential direction Q_s, non-dimensionalised with $\pi R^2U_tOh^{-0.12}$, plotted against the dimensionless time t/t_{bc}. — (black), $Q_T/2\pi RZ_cU_c = 1$; — (red), $Q_b(t)/2\pi Z_cRU_c = 0.5\cos^2(0.42\pi t/t_{bc})$; — (blue), $Q_s(t)/\pi R^2U_tOh^{-0.12} = 0.13 + 0.15\sin^2(0.5\pi t/t_{bc})$. Symbols with dots represent the volume influx in the (bottom) normal direction Q_b. The rest of the symbols are the same as in figure 12.

and $\phi_0 \approx \theta$ (see figure 2*d*) is the phase angle when the cavity opens. In the inset of figure 13 the dimensionless side volume flux $Q_s/\pi R^2U_tOh^{-0.12}$ is plotted against the dimensionless time t/t_{bc}. Equation (4.1) collapses the data, with the final expression based on the data fit being

$$\frac{Q_s(t)}{\pi R^2U_tOh^{-0.12}} = 0.12 + 0.15\sin^2\left(\frac{0.5\pi t}{t_{bc}}\right). \tag{4.2}$$

The first term on the right-hand side of (4.2), the y-intercept in the inset of figure 13, is interpreted as the initial side flux. The usage of a y-intercept was necessary because of the lack of experimental data around the initial time $t = 0$.

We now consider the scaling of the bottom flux. The characteristic area below the kink is $2\pi R\bar{z}(t)$, where $\bar{z}(t)$ is the vertical distance between the kink and the cavity bottom (see figure 11*b*). The velocity of shrinking in the equatorial plane follows the capillary velocity (see (3.17)). Hence, the normal influx below the kink is $Q_b \sim 2\pi R\bar{z}(t)U_c \sim 2\pi RU_c(Z_c - R(1-\cos\phi))$. Taking $2R/Z_c \approx 1$ for small Bo (Puthenveettil *et al.* 2018) results in the simplified relation

$$\frac{Q_b}{2\pi RZ_cU_c} \approx a_2\cos^2(\phi/2), \tag{4.3}$$

where a_2 is a numerical prefactor. Figure 13 shows that (4.3) collapses the Q_b data at various Bo and Oh, with the best fit relation for the non-dimensional bottom flux, $Q_b(t)/2\pi RZ_cU_c$, shown in figure 13 being

$$\frac{Q_b(t)}{2\pi RZ_cU_c} = 0.5\cos^2\left(\frac{0.42\pi t}{t_{bc}}\right). \tag{4.4}$$

The phase angle of Q_s in (4.2), πt, is slightly larger than that of Q_b in (4.4), $0.84\pi t$, an artefact of the side flux area being at the top of the bottom flux area.

We now assume that the retracting rim solely creates a wave-like propagating disturbance without causing any effective mass transfer down the cavity. Then, the total cavity filling rate $Q_T \approx (Q_b + Q_s)|_{t\to 0} \approx 2\pi R Z_c U_c$. This means that the initial side flux in (4.2) is then due to the normal shrinking. Figure 13 shows that $Q_T/2\pi R Z_c U_c$ collapses the data reasonably well. From the plot, the equation of best fit is

$$\frac{Q_T(t)}{2\pi R Z_c U_c} \approx 1, \tag{4.5}$$

validating our assumptions to arrive at the above relation.

Equation (4.5) shows that the total volume flux is entirely due to the normal shrinkage velocity of the cavity. When $Bo < 0.1$, the normalised cavity depth $Z_c/R \to 2$ (Puthenveettil *et al.* 2018), and is independent of Bo. Then, $Q_T \simeq 4\pi R^2 U_c$, so that gravity effects in Q_T becomes negligible. Gravity effects become significant in Q_T through the Bo dependency of Z_c, given by (C1), in the moderate to large bubble size range ($Bo > 0.1$). As we show in Appendix A, towards $t = t_{bc}$, when the cavity becomes conical, if we assume that the total mass flux ρQ_T, where Q_T is given by (4.5), initiates a jet by momentum exchange, we then retrieve the observed jet velocity scaling.

5. Conclusions

The disintegration of the thin film at the top of the floating bubble, and the rim retraction that follows, leads to the formation of a kink (intersection of the concave with the convex cavity boundary) that propagates as a capillary wave with a velocity U_t tangentially along the cavity boundary. Precursory capillary waves move ahead of this kink. Simultaneously, the cavity shrinks with a normal velocity U_n due to the sudden reduction of the gas pressure after the film rupture. The tangential motion of the kink, combined with the overall inward shrinkage of the cavity due to reduction in gas pressure is a unique feature of surface bubble cavity collapse, not encountered in open cavity collapse problems as treated by Zeff *et al.* (2000), Bergmann *et al.* (2006), Bartolo *et al.* (2006), Duclaux *et al.* (2007), Das & Hopfinger (2008), Benusiglio, Quéré & Clanet (2014), Thoroddsen *et al.* (2018), Yang, Tian & Thoroddsen (2020) and Krishnan, Bharadwaj & Vasan (2022).

An increase in fluid viscosity increases the tangential kink velocity because of the progressive damping of the precursory capillary waves, with complete damping occurring when $Oh = 0.02$. Using an energy model of the main wave upstream of the kink, we show that $U_t \approx 4.5 U_c \mathcal{W}_R$ (3.14), where U_c is the capillary velocity, $\mathcal{W}_R = (1 - \sqrt{Oh\mathscr{L}})^{-1/2}$ (3.15) is the wave resistance factor, with $\mathscr{L}(Bo) = \pi - R_r/R$ (3.8) being the correction for the path length of the travel of the kink, Oh the Ohnesorge number, Bo the Bond number and R_r the rim radius.

The sudden release of compressed gas from the bubble cavity, immediately after the thin film rupture, causes an overall inward shrinking of the cavity. It produces a normal velocity component of the kink. In the horizontal equatorial plane, the normal velocity scales with U_c (3.17), devoid of viscous and gravity effects. In contrast, the bottom part of the cavity shrinks vertically upwards with a velocity $U_c(Z_c/R)\mathcal{W}_R\mathscr{L}^{-1}$ (3.19). The viscous effect on the vertical shrinkage at the bottom, $\mathcal{W}_R$, is due to the deformations by the precursory capillary waves on the cavity. The gravity effect on this shrinkage originates from the initial static geometry of the cavity, indicated by the aspect ratio of the cavity Z_c/R, and the path correction $\mathscr{L}$.

The total time of cavity collapse is shown to scale as $t_{bc} \approx 0.13 t_c \mathscr{L}$ (3.10) with the gravity dependency being due to the Bo-dependency of the kink trajectory $\mathscr{L}$. This leads to the understanding that the damping of the precursory capillary waves follows a modified relation $\lambda/R \approx Oh^{1/2}\mathscr{L}^{1/2}$ (3.12), indicating that the damping slightly decreases with an increase in Bond number.

The mass flux of cavity filling, ρQ_T, consists of a sum of the side flux ρQ_s and the normal bottom flux ρQ_b. We show that $Q_T \approx 2\pi R Z_c U_c$ (4.5), which, through its dependence on the aspect ratio of the cavity Z_c/R, is a function of Bo. The entire magnitude of ρQ_T originates from the normal shrinkage of the cavity, confirming that the kink movement, initiated by the rim retraction, is a wave propagation with no effective mass transfer. Indeed, the tangential velocity U_t, which is constant with respect to time for a given bubble, corresponds closely to the phase velocity of a capillary wave of wavelength λ, i.e. $U_t \approx c_p$ (3.16), where $c_p = (2\pi)^{1/2}\sqrt{\sigma/\rho\lambda}$. With the experimental value of $\lambda/R \approx 0.36$, we get $c_p \approx 4.2U_c$, which is close to U_t (3.14), neglecting the weak dependency on viscosity and gravity. The role of outflux Q_o in the cavity collapse has not been analysed in this paper. This outflux becomes relevant in deciding the far field conditions at the free surface, and hence, can potentially influence the flow field around the cavity interface.

At the bottom of the cavity, there is an exchange of momentum, via pressure build-up, between the mass flux ρQ_T of the cavity and the initial mass flux of the jet, $\rho\pi {r_b}^2 U_j$, where r_b is the base radius of the cavity and U_j the jet velocity (see Appendix A). This exchange gives a jet Weber number scaling of $(U_j/U_c)^2 \sim (Z_c R/{r_b}^2)^2$, the same scaling relation as proposed by Krishnan *et al.* (2017).

Supplementary movies. Supplementary movies are available at https://doi.org/10.1017/jfm.2024.26.

Funding. The authors would like to acknowledge the partial financial support from DST, Government of India, under the FIST Grants SR/FST/ETII-017/2003, SR/FST/ETII-064/2015 and the Core Research Grants SR/S3/MERC/028/2009, CRG/2021/007497 for this study.

Declaration of interests. The authors report no conflict of interest.

Author ORCIDs.
Sangeeth Krishnan https://orcid.org/0000-0002-5854-3214;
Baburaj A. Puthenveettil https://orcid.org/0000-0002-8694-4322.

Appendix A. Momentum balance at the cavity bottom

Deike *et al.* (2018) and Duchemin *et al.* (2002) observed in their numerical simulations, two successive velocity (or pressure) peaks at the cavity bottom, with the second peak being the highest. Considering the initial peak to be due to the capillary waves, and the second one to be due to the kink, the momentum of the precursor waves is then not significant, compared with that of the kink, an aspect clarified by Gañán Calvo (2018). However, the volume flux (or mass flux) is associated with the capillary velocity U_c due to the normal shrinking of the cavity (see (4.5)), while U_t is only a propagation velocity, carrying little mass. The rate of change of momentum of the liquid of the collapsing cavity is then $\mathrm{d}(mU_c)/\mathrm{d}t$, where m is the associated liquid mass. Differentiation gives $\dot{m}U_c + m\dot{U}_c$, where $\dot{m}$ is the mass flux of the cavity collapse. Since U_c is a constant with respect to time, we get

$$\frac{\mathrm{d}}{\mathrm{d}t}(mU_c) = \dot{m}U_c. \tag{A1}$$

The momentum flux in (A1) will appear as a force during the axisymmetric flow-convergence at the cavity bottom. The corresponding pressure build-up is

$$p \simeq \dot{m} U_c / 2\pi {r_b}^2, \tag{A2}$$

where $2\pi {r_b}^2$ is the characteristic area at the base of the cavity of bottom radius r_b (see figure 2*d*). The radius r_b is a characteristic value, which is an upper limit of the cavity bottom radius, which decreases with time during the flow convergence. The reader is referred to Eggers *et al.* (2007), Eggers & Fontelos (2015) and to the recent work of Gañán Calvo & López-Herrera (2021) for detailed discussions on the dynamics of the local cylindrical collapse within the length scale r_b, at the cavity bottom. By substituting the total mass influx $\dot{m} = \rho Q_T$ from (4.5) in (A2), we get an estimate of the pressure at the bottom of the cavity at flow convergence as

$$p \simeq \left(\frac{Z_c}{R}\right) \rho {U_c}^2 \left(\frac{R}{r_b}\right)^2. \tag{A3}$$

Equation (A3) shows that the pressure build-up at the bottom of the cavity, has primarily a capillary–inertial scaling, of the form $\rho {U_c}^2$. As the aspect ratio of the cavity Z_c/R is a function of Bo, as given by (C1) (Puthenveettil *et al.* 2018), p also depends on Bo. Similarly, the effect of precursory capillary waves on p is accounted for by the term $(R/r_b)^2$ in (A3). As we discuss later, a reduced area of impact, due to lower r_b in the absence of capillary waves, increases the impact pressure.

The pressure impulse of the impact $I = \int_{t_i}^{t_f} p \, \mathrm{d}t$, where the subscripts i and f denote the initial and the final values of time t, is estimated to be

$$I \approx p \Delta t, \tag{A4}$$

where $\Delta t = t_f - t_i$ is the characteristic time scale of the impact. The natural choice of this time scale of impact, since the flow convergence is capillary driven, is

$$\Delta t \simeq r_b / U_c. \tag{A5}$$

The vertical jet velocity is

$$U_j = -\boldsymbol{\nabla}(I/\rho), \tag{A6}$$

since the gradient of pressure impulse drives the jet in the axial direction. Substituting (A3) and (A5) in (A4) and the resulting expression for I in (A6), we obtain

$$U_j \simeq \boldsymbol{\nabla} \left(\frac{R Z_c U_c}{r_b}\right). \tag{A7}$$

Approximating the gradient operator $\boldsymbol{\nabla}$ as $1/r_b$, gives the jet Weber number We_j as

$$We_j = \left(\frac{U_j}{U_c}\right)^2 \sim \left(\frac{Z_c}{R}\right)^2 \left(\frac{R}{r_b}\right)^4, \tag{A8}$$

with the ratio R/r_b depending on the presence, or absence, of the precursor capillary waves. The presence of precursory capillary waves in low Oh results in a larger cavity base radius r_b (see figure 3*i*), in comparison with that at larger Oh (see figure 4*i*).

Figure 14 shows the measurements of r_b, non-dimensionalised with R, and corrected using an Oh factor to account for the precursory capillary waves effect, plotted as a function of Bo. The figure shows that the data falls on to a horizontal line, indicating a

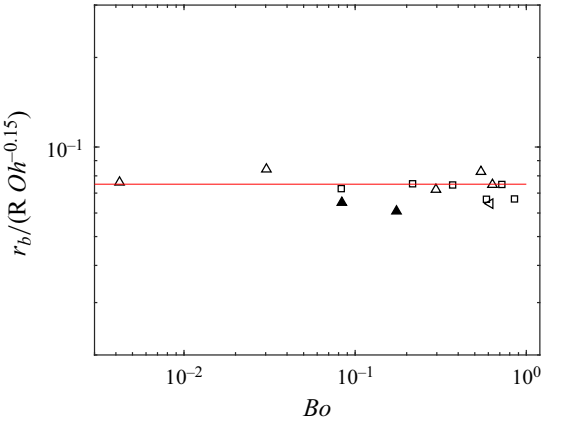

Figure 14. Variation of the dimensionless bottom radius (r_b/R) of the cavity, with an Oh correction, with the Bond number Bo. △, water; ◁, ethanol; ▲, GW48 (30 °C); □, GW55; —, $r_b = 0.075\ R\ Oh^{-0.15}$.

linear dependence of r_b with the bubble radius R, and that the vertical offsets between the data sets due to precursory capillary waves are reduced by using an $Oh^{-0.15}$ factor. The best fit power law relation, shown as the solid line in the figure, is

$$r_b \approx 0.1ROh^{-0.15}, \tag{A9}$$

which is valid for $0.002 < Oh < 0.035$ and $10^{-3} < Bo < 1$. Substituting (A9) in (A8), yields

$$We_j \sim (Z_c/R)^2 Oh^{0.6}, \tag{A10}$$

which is the same scaling as that proposed by Krishnan *et al.* (2017), with a small variation in the exponent of Oh.

Appendix B. Sudden rise in normal velocity U_n

The rise in normal velocity at the bottom of the cavity, observed in low-viscosity fluids in figure 8, is due to the convergence of precursory capillary waves at the bottom of the cavity, and the subsequent momentum exchange at the interface. These higher velocities can be obtained as in the case of an analogous problem of waves on the surface of a drop impacting a solid surface, studied by Renardy *et al.* (2003). During wave focusing at the bottom of the cavity, the local cylindrical radius of the cavity $r \simeq \lambda$, where λ is the wavelength. The inward pull due to the unbalanced surface tension along the azimuthal direction is $F_\sigma = 2\pi\lambda\sigma$. The rate of change of momentum of the interface $\mathrm{d}P/\mathrm{d}t = \pi\rho\lambda^3 V_b/t_{c\lambda}$, where the time scale over which the momentum changes $t_{c\lambda} = \sqrt{\rho\lambda^3/\sigma}$, and V_b is the normal velocity at the bottom of the cavity. Equating $\mathrm{d}P/\mathrm{d}t$ with F_σ results in an approximate estimate of the higher values of the normal velocity at the bottom of the cavity as $V_b \simeq 2\sqrt{\sigma/\rho\lambda}$. Substituting $\lambda \approx 0.4R$ (Krishnan *et al.* (2017)) in V_b, an order of magnitude higher value of velocity, in comparison with (3.19), is obtained.

Appendix C. Solution for $Z_c(Bo)$ by Puthenveettil *et al.* (2018)

The closed form solution for the dimensionless cavity depth, when $Bo \leq 1$, is expressed as

$$\frac{Z_c(Bo)}{R} = \mathscr{F} - \frac{\chi\xi(\mathscr{F} + 2/Bo)}{16 + 8\chi\xi\sqrt{Bo} + \xi^2(4 + Bo(\chi^2 + 4\mathscr{F}) + Bo^2\mathscr{F}^2)}, \tag{C1}$$

where $\chi = \mathrm{K}_0((R_r/R)Bo^{1/2})/\mathrm{K}_1((R_r/R)Bo^{1/2})$, $\xi = (1 - (\mathscr{G} - \mathscr{H} - (1/3)))^{1/2}$ and $\mathscr{F} = 1 + (\mathscr{G} - \mathscr{H} - (1/3))^{1/2}$. Here, R_r/R is the dimensionless rim radius given by (3.9), K_0 is the modified Bessel function of the second kind of order zero, K_1 is the first derivative of K_0 with respect to its argument, $\mathscr{G} = 2(1/Bo + 1/Bo^2)$, and $\mathscr{H} = (-4/(3Bo^2) + 8/Bo^3 + 4/Bo^4)^{1/2}$.

References

Bartolo, D., Josserand, C. & Bonn, D. 2006 Singular jets and bubbles in drop impact. *Phys. Rev. Lett.* **96**, 124501.

Benusiglio, A., Quéré, D. & Clanet, C. 2014 Explosions at the water surface. *J. Fluid Mech.* **752**, 123–139.

Bergmann, R., van der Meer, D., Stijnman, M., Sandtke, M., Prosperetti, A. & Lohse, D. 2006 Giant bubble pinch-off. *Phys. Rev. Lett.* **96**, 154505.

Blanchard, D.C. 1963 The electrification of the atmosphere by particles from bubbles in the sea. *Prog. Oceanogr.* **1**, 71–202.

Blanco-Rodríguez, F.J. & Gordillo, J.M. 2020 On the sea spray aerosol originated from bubble bursting jets. *J. Fluid Mech.* **886**, R2.

Blanco-Rodríguez, F.J. & Gordillo, J.M. 2021 On the jets produced by drops impacting a deep liquid pool and by bursting bubbles. *J. Fluid Mech.* **916**, A37.

Boulton-Stone, J.M. & Blake, J.R. 1993 Gas bubbles bursting at a free surface. *J. Fluid Mech.* **254**, 437–466.

Brasz, C.F., Bartlett, C.T., Walls, P.L.L., Flynn, E.G., Yu, Y.E. & Bird, J.C. 2018 Minimum size for the top jet drop from a bursting bubble. *Phys. Rev. Fluids* **3**, 074001.

Burton, J.C., Waldrep, R. & Taborek, P. 2005 Scaling and instabilities in bubble pinch-off. *Phys. Rev. Lett.* **94** (18), 184502.

Das, S.P. & Hopfinger, E.J. 2008 Parametrically forced gravity waves in a circular cylinder and finite-time singularity. *J. Fluid Mech.* **599**, 205–228.

Deike, L., Ghabache, E., Liger-Belair, G., Das, A.K., Zaleski, S., Popinet, S. & Séon, T. 2018 Dynamics of jets produced by bursting bubbles. *Phys. Rev. Fluids* **3**, 013603.

Doshi, P., Cohen, I., Zhang, W.W., Siegel, M., Howell, P., Basaran, O.A. & Nagel, S.R. 2003 Persistence of memory in drop breakup: the breakdown of universality. *Science* **302** (5648), 1185–1188.

Duchemin, L., Popinet, S., Josserand, C. & Zaleski, S. 2002 Jet formation in bubbles bursting at a free surface. *Phys. Fluids* **14** (9), 3000–3008.

Duclaux, V., Caille, F., Duez, C., Ybert, C., Bocquet, L. & Clanet, C. 2007 Dynamics of transient cavities. *J. Fluid Mech.* **591**, 1–19.

Eggers, J. & Fontelos, M.A. 2015 *Singularities: Formation, Structure, and Propagation*. Cambridge University Press.

Eggers, J., Fontelos, M.A., Leppinen, D. & Snoeijer, J.H. 2007 Theory of the collapsing axisymmetric cavity. *Phys. Rev. Lett.* **98** (9), 094502.

Feng, J., Roché, M., Vigolo, D., Arnaudov, L.N., Stoyanov, S.D., Gurkov, T.D., Tsutsumanova, G.G. & Stone, H.A. 2014 Nanoemulsions obtained via bubble-bursting at a compound interface. *Nat. Phys.* **10** (8), 606–612.

Gañán Calvo, A.M. 2017 Revision of bubble bursting: universal scaling laws of top jet drop size and speed. *Phys. Rev. Lett.* **119**, 204502.

Gañán Calvo, A.M. 2018 Scaling laws of top jet drop size and speed from bubble bursting including gravity and inviscid limit. *Phys. Rev. Fluids* **3**, 091601.

Gañán Calvo, A.M. & López-Herrera, J.M. 2021 On the physics of transient ejection from bubble bursting. *J. Fluid Mech.* **929**, A12.

Gañán-Calvo, A.M. 2023 The ocean fine spray. *Phys. Fluids* **35** (2), 023317.

GHABACHE, E., ANTKOWIAK, A., JOSSERAND, C. & SÉON, T. 2014 On the physics of fizziness: how bubble bursting controls droplets ejection. *Phys. Fluids* **26** (12), 121701.
GORDILLO, J.M. & BLANCO-RODRÍGUEZ, F.J. 2023 Theory of the jets ejected after the inertial collapse of cavities with applications to bubble bursting jets. *Phys. Rev. Fluids* **8**, 073606.
GORDILLO, J.M. & RODRÍGUEZ-RODRÍGUEZ, J. 2019 Capillary waves control the ejection of bubble bursting jets. *J. Fluid Mech.* **867**, 556–571.
ISMAIL, A.S., GAÑÁN CALVO, A.M., CASTREJÓN-PITA, J.R., HERRADA, M.A. & CASTREJÓN-PITA, A.A. 2018 Controlled cavity collapse: scaling laws of drop formation. *Soft Matt.* **14**, 7671–7679.
JI, B., YANG, Z. & FENG, J. 2021 Compound jetting from bubble bursting at an air–oil–water interface. *Nat. Commun.* **12** (1), 6305.
JOUNG, Y.S., GE, Z. & BUIE, C.R. 2017 Bioaerosol generation by raindrops on soil. *Nat. Commun.* **8**, 14668.
KIENTZLER, C.F., ARONS, A.B., BLANCHARD, D.C. & WOODCOCK, A.H. 1954 Photographic investigation of the projection of droplets by bubbles bursting at a water surface. *Tellus* **6** (1), 1–7.
KRISHNAN, S., BHARADWAJ, S.V. & VASAN, V. 2022 Impact of freely falling liquid containers and subsequent jetting. *Exp. Fluids* **63** (7), 1–20.
KRISHNAN, S., HOPFINGER, E.J. & PUTHENVEETTIL, B.A. 2017 On the scaling of jetting from bubble collapse at a liquid surface. *J. Fluid Mech.* **822**, 791–812.
KRISHNAN, S. & PUTHENVEETTIL, B.A. 2015 Dynamics of collapse of free surface bubbles. *Procedia IUTAM* **15**, 207–214.
KRISHNAN, S., PUTHENVEETTIL, B.A. & HOPFINGER, E.J. 2020 Hole expansion from a bubble at a liquid surface. *Phys. Fluids* **32** (3), 032108.
LAI, C.Y., EGGERS, J. & DEIKE, L. 2018 Bubble bursting: universal cavity and jet profiles. *Phys. Rev. Lett.* **121**, 144501.
LEE, J.S., WEON, B.M., PARK, S.J., JE, J.H., FEZZAA, K. & LEE, W.K. 2011 Size limits the formation of liquid jets during bubble bursting. *Nat. Commun.* **2**, 367.
LIGHTHILL, J. 1978 *Waves in Fluids*. Cambridge University Press.
MACINTYRE, F. 1972 Flow patterns in breaking bubbles. *J. Geophys. Res.* **77** (27), 5211–5228.
OGUZ, H.N. & PROSPERETTI, A. 1993 Dynamics of bubble growth and detachment from a needle. *J. Fluid Mech.* **257**, 111–145.
PERLIN, M., LIN, H. & TING, C.L. 1993 On parasitic capillary waves generated by steep gravity waves: an experimental investigation with spatial and temporal measurements. *J. Fluid Mech.* **255**, 597–620.
PUTHENVEETTIL, B.A. & HOPFINGER, E.J. 2009 Evolution and breaking of parametrically forced capillary waves in a circular cylinder. *J. Fluid Mech.* **633**, 355–379.
PUTHENVEETTIL, B.A., SAHA, A., KRISHNAN, S. & HOPFINGER, E.J. 2018 Shape parameters of a floating bubble. *Phys. Fluids* **30** (11), 112105.
RENARDY, Y., POPINET, S., DUCHEMIN, L., RENARDY, M., ZALESKI, S., JOSSERAND, C., DRUMRIGHT-CLARKE, M.A., RICHARD, D., CLANET, C. & QUÉRÉ, D. 2003 Pyramidal and toroidal water drops after impact on a solid surface. *J. Fluid Mech.* **484**, 69–83.
SAMPATH, K., AFSHAR-MOHAJER, N., CHANDRALA, L.D., HEO, W.S., GILBERT, J., AUSTIN, D., KOEHLER, K. & KATZ, J. 2019 Aerosolization of crude oil-dispersant slicks due to bubble bursting. *J. Geophys. Res.* **124** (10), 5555–5578.
SPIEL, D.E. 1995 On the births of jet drops from bubbles bursting on water surfaces. *J. Geophys. Res.* **100** (C3), 4995–5006.
THORODDSEN, S.T., TAKEHARA, K., NGUYEN, H.D. & ETOH, T.G. 2018 Singular jets during the collapse of drop-impact craters. *J. Fluid Mech.* **848**, R3.
WALLS, P.L.L., HENAUX, L. & BIRD, J.C. 2015 Jet drops from bursting bubbles: how gravity and viscosity couple to inhibit droplet production. *Phys. Rev.* E **92**, 021002.
WALLS, P.L.L., MCRAE, O., NATARAJAN, V., JOHNSON, C., ANTONIOU, C. & BIRD, J.C. 2017 Quantifying the potential for bursting bubbles to damage suspended cells. *Sci. Rep.* **7** (1), 15102.
WOODCOCK, A.H., KIENTZLER, C.F., ARONS, A.B. & BLANCHARD, D.C. 1953 Giant condensation nuclei from bursting bubbles. *Nature* **172**, 1144–1145.
YANG, Z., JI, B., AULT, J.T. & FENG, J. 2023 Enhanced singular jet formation in oil-coated bubble bursting. *Nat. Phys.* **19**, 1–7.
YANG, Z.Q., TIAN, Y.S. & THORODDSEN, S.T. 2020 Multitude of dimple shapes can produce singular jets during the collapse of immiscible drop-impact craters. *J. Fluid Mech.* **904**, A19.
ZEFF, B.W., KLEBER, B., FINEBERG, J. & LATHROP, D.P. 2000 Singularity dynamics in curvature collapse and jet eruption on a fluid surface. *Nature* **403** (6768), 401–404.